Int J Adv Manuf Technol (2010) 46:491–507
DOI 10.1007/s00170-009-2117-5

ORIGINAL ARTICLE

An experimental and coupled thermo-mechanical finite element study of heat partition effects in machining

Fazar Akbar · Paul T. Mativenga · M. A. Sheikh

Received: 14 June 2008 / Accepted: 18 May 2009 / Published online: 2 June 2009

Abstract A better understanding of heat partition between the tool and the chip is required in order to produce more realistic finite element (FE) models of machining processes. The objectives are to use these FE models to optimise the cutting process for longer tool life and better surface integrity. In this work, orthogonal cutting of AISI/SAE 4140 steel was performed with tungsten-based cemented carbide cutting inserts at cutting speeds ranging between 100 and 628 m/min with a feed rate of 0.1 mm/rev and a constant depth of cut of 2.5 mm. Cutting temperatures were measured experimentally using an infrared thermal imaging camera. Chip formation was simulated using a fully coupled thermo-mechanical finite element model. The results from cutting tests were used to validate the model in terms of deformed chip thickness and cutting forces. The coupled thermo-mechanical model was then utilised to evaluate the sensitivity of the model output to the specified value of heat partition. The results clearly show that over a wide range of cutting speeds, the accuracy of finite element model output such as chip morphology, tool–chip interface temperature, von Mises stresses and the tool–chip contact length are significantly dependent on the specified value of heat partition.

Keywords Heat partition · Thermo-mechanical modelling · Finite element method · Chip formation

1 Introduction

An understanding of the material removal process is necessary when aiming to increase the dimensional accuracy and the surface integrity of a machined product. To enhance product dimensional accuracy and surface integrity, the effect of heat partition (into the cutting tool and the chip during cutting) on the deformation of the machined workpiece, the chip shape, the cutting force and the stress distribution must be understood. Although there have been numerous studies on orthogonal cutting, little research effort has been made in exploring the effects on the cutting process of heat partition into the cutting tool. In this research work, finite element method (FEM) has been used to simulate chip formation in the machining process. The validated model is then used to predict machining attributes which are affected by heat partition.

1.1 A review of previous work on heat partition between the tool and the chip

The heat that flows into the cutting tool during dry turning is an important factor which influences tool wear mechanisms, tool performance and quality of the machined part. Blok's principle [1] has been widely used in the analytical investigation of temperatures generated in metal cutting. It models two bodies, one stationary and the other moving with a relative velocity. This principle can be employed to solve the problem of heat partition at the tool–chip interface by matching the temperature between the chip and the tool. Chao and Trigger [2] used Blok's partition principle, but were not successful in achieving an interface temperature rise on the chip in agreement with that on the tool. Komanduri and Hou [3] furthered the functional analysis approach based on the idea of Chao and Trigger [2]. Huang and Liang [4] used a non-uniform heat intensity along the tool–chip interface in their model and determined heat partition using the lengths of sticking and sliding zones from other studies. Karpat and Ozel [5, 6] determined heat partition based on a non-uniform heat intensity and calculated the actual lengths of sticking and sliding zones empirically for a carbide tool.

F. Akbar (✉) · P. T. Mativenga · M. A. Sheikh
School of Mechanical, Aerospace and Civil Engineering,
The University of Manchester,
Sackville Street Building,
Manchester M60 1QD, UK
e-mail: faraz.akbar@postgrad.manchester.ac.uk

Reported numerical values for heat partition in machining are summarised in Table 1. According to Loewen and Shaw [7], heat transmitted into the tool varies between 40% and 20% when machining SAE B1113 free cutting steel with a K2S carbide tool at cutting speeds of 30 to 182 m/min. Takeuchi et al. [8] have reported that 10% to 30% of the total heat generated enters the tool. They applied this assumption in machining of carbon steel (C=0.55%) using P15 carbide tooling at a cutting speed of 100 m/min. According to Wright et al. [9], 10% to 20% of heat generated at the rake face flows into the tool when machining annealed low carbon iron with M34 high-speed steel at cutting speeds ranging from 10 to 175 m/min. Casto et al. [10] reported that between 56% and 24% of heat was transmitted into the tool when machining AISI 1040 with a P10 sintered carbide insert at cutting speeds of 99 to 240 m/min. Grzesik and Nieslony [11] estimated that the fraction of heat going into the tool varied from 35% to 20% when using multilayer coated tools, but changed from 50% to 40% for uncoated carbide tools in the range of cutting speeds of 50 to 210 m/min for the workpiece material AISI 1045. Abukhshim et al. [12] evaluated the heat partition coefficient for the tool in machining of AISI/SAE 4140 steel using P20 carbide tools to vary between 50% and 15% in conventional machining at cutting speeds of 200 to 600 m/min.

From Table 1, it is also noted that most researchers have assumed for the FEM models the value of heat partition into the cutting tool and chip as 50% [13–27]. Mabrouki and Rigal [28] calculated the heat partition into the cutting tool as 65% and used this value in their simulations when using the ABAQUS software to model the turning of AISI 4340 steel. Ng et al. [29] used heat partition into the cutting tool as 48% and 59% and used these values in their simulations using the code FORGE2 to model the turning of hardened AISI H13 in which continuous chips were obtained. Zong et al. [30] calculated the heat partition into the diamond tool as 72% and used this value in their simulations when using the updated Lagrangian formulation to simulate the turning of OFHC copper. Mohamed et al. [31] calculated heat partition value analytically between the tool and the chip to be 60% and 40%, respectively, and used these values in their simulations when using the ABAQUS software to model the turning of AISI 316L steel.

Machining is a coupled thermo-mechanical process. Although there are many significant studies [16, 17, 32–35] presenting different methodologies in studying chip formation, there are only a few focussing on thermo-mechanical effects. Additionally, in finite element modelling of the machining process, most researchers assume that heat partition into the cutting tool and the chip is equal, as shown in Table 1. This has been supported by the fact that heat partition into the tool and the chip has not always been considered as a crucial input to FE models.

In this paper, an explicit two-dimensional FE model has been developed to analyse turning of AISI/SAE 4140 steel using a carbide cutting tool. Heat partition obtained from matching FE temperatures with experimentally measured temperatures is used in a coupled thermo-mechanical model. Orthogonal cutting experiments are used to validate the model in terms of deformed chip thickness and cutting forces. The validated FE model is then used to study the sensitivity of heat partition values.

2 Experimental investigations

2.1 Experimental details

The cutting tests were performed on a Dean Smith and Grace Lathe machine. A Kistler cutting force dynamometer model 9263 was used to measure the cutting forces. The inserts used were tungsten-based uncoated cemented carbide, Sandvik grey which have geometry designated as TCMW 16T304 (ISO grade P10; triangular shape insert with 0.4-mm nose radius, 3.97-mm thickness and 7° clearance angle). Inserts without chip breaker were selected so that the tool–chip contact length was not constrained. The tool holder used was Sandvik STGCR 2020K-16.

A pre-bored workpiece made of AISI/SAE 4140 (23.9 HRC) high tensile strength alloy steel was used with an external diameter of 200 mm and 2.5-mm tube thickness. The experimental setup is shown in Fig. 1. The orthogonal cutting arrangement was such that the tool approach angle was 90° and the undeformed chip thickness was equal to the feed rate. The depth of cut was set by the thickness of the pre-bored workpiece material. A close-up view of the triangular insert and workpiece is shown in Fig. 1. Due to the dynamic nature of the cutting process, the chip is not displayed. The cutting tests were performed at six different cutting speeds of 100, 197, 314, 395, 565 and 628 m/min. These cutting speeds were set by the available revolution per minute on the conventional lathe. A new cutting edge was used for every cutting speed. The feed rate and depth of cut were kept constant at 0.1 mm/rev and 2.5 mm, respectively. The process parameters, as summarised in Table 2, were selected as appropriate to the cutting tests for the highest cutting speed used.

2.2 Experimental temperature measurements

Various experimental techniques have been developed and utilised to study cutting temperatures [36–44]. It appears from literature that infrared thermal imaging is a useful technique for obtaining temperature distributions in cutting. In the current work, temperatures are measured using an

Table 1 Heat partition values as used in FEM models

Authors and reference	Workpiece material	Cutting tool material	Cutting velocity (m/min)	Heat partition into the cutting tool (R_T)	FE software
Loewen and Shaw [7]	SAE B1113 Steel	K2S carbide	30 to 182	40% down to 20% (calculated analytically)	–
Takeuchi et al. [8]	Carbon steel (C=0.55%)	P15 carbide	100	10–30% (assumed)	–
Wright et al. [9]	Low-carbon iron	M34 high-speed steel	10–175	10–20%	–
Casto et al. [10]	AISI 1040	Sintered carbide type P10	99–240	56% down to 24%	ALGOR
Grzesik and Nieslony [11]	AISI 1045	Multilayer coating	50–210	35% down to 20% (Calculated analytically)	–
Grzesik and Nieslony [11]	AISI 1045	P20 uncoated carbide	50–210	50% down to 40% (Calculated analytically)	–
Abukhshim et al. [12]	AISI 4140	Uncoated carbide	200–600	46% down to 15%	ANSYS 7.1/ Standard
Shih [13]	AISI 1020	High-speed steel	35	50% (assumed)	–
Lei et al. [14]	AISI 1020	tungsten carbide	240	50% (Assumed)	ABAQUS
Xie et al. [15]	AISI 1045	Uncoated carbide WC-Co	300	50% (assumed)	ABAQUS
Arrazola et al. [16]	AISI 4140	C. C. grade P10	300	50% (assumed)	ABAQUS/Explicit
Arrazola et al. [17]	AISI 4140	P10	200–600	50% (assumed)	ABAQUS/Explicit
Reginaldo et al. [18]	AISI 4340	PCBN substrate with TiAlN coating	150	50% (assumed)	
Shet and Deng [19]	AISI 4340	–	152	50% (assumed)	ABAQUS
Shet et al. [20]	AISI 4340	–	152	50% (assumed)	ABAQUS
Shi et al. [21]	AISI 4340	–	152	50% (assumed)	ABAQUS
Shet and Deng [22]	AISI 4340	–	152	50% (Assumed)	ABAQUS
Shi and Liu [23]	AISI 52100	Polycrystalline cubic boron nitride (PCBN)	182	50% (assumed)	ABAQUS/Explicit
Shi and Liu [24]	AISI 52100	SPG-422 (PCBN)	107	50% (assumed)	ABAQUS/Explicit
Kai and Melkote [25]	AI5083-H116	Single crystal and Polycrystalline diamond tools	10 and 200	50% (assumed)	ABAQUS/Standard
Shi and Liu [26]	HY-100	TPG 322 inserts	107	50% (assumed)	ABAQUS/Explicit
Li et al. [27]	Oil hardening O1 steel	Flat and two types of cratered tools	244	50% (assumed)	ABAQUS
Mabrouki and Rigal [28]	AISI 4340	Tungsten carbide	100	65% (calculated analytically)	ABAQUS/Explicit
Ng et al. [29]	AISI H13	polycrystalline cubic boron nitride	75, 150 and 200	48% and 59% (calculated analytically)	FORGE2
Zong et al. [30]	OFHC copper	diamond tool	6, 30, 60 and 120	72% (calculated analytically)	–
Mohamed et al. [31]	AISI 316L	Kennametal K313	125	60% (calculated analytically)	ABAQUS/Explicit

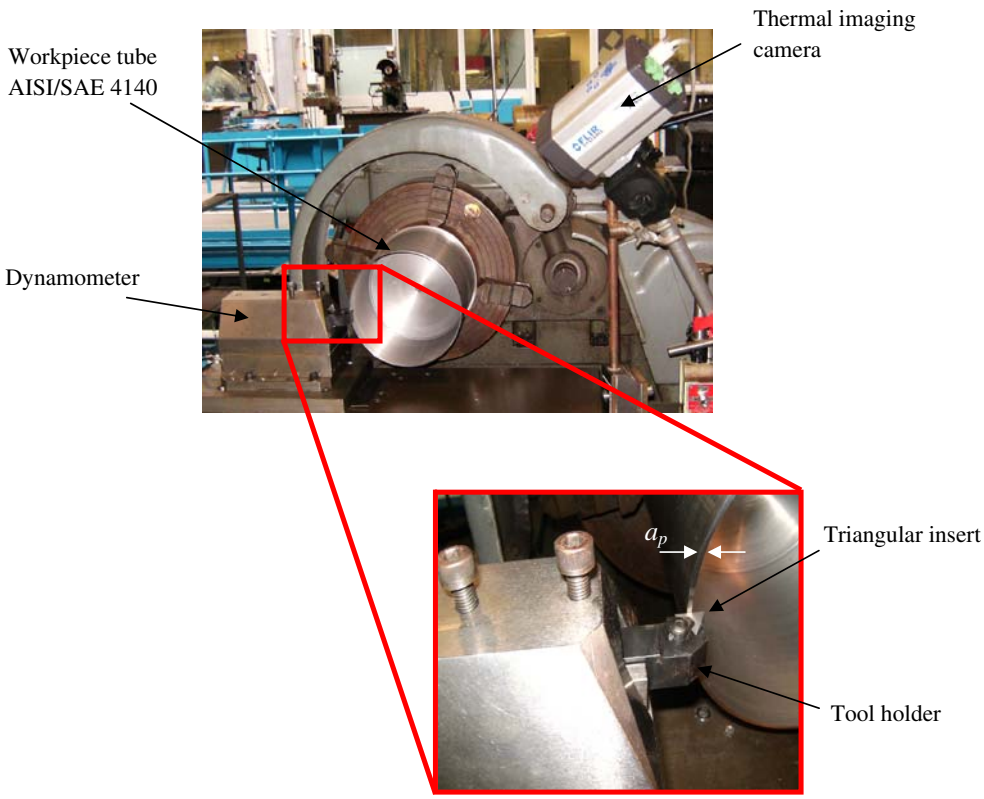

Fig. 1 Experimental setup

infrared (IR) thermal imager FLIR ThermaCAM® SC3000, a long wave and self-cooling analysis system. This package allows extensive analysis of highly dynamic objects and events typically found in metal machining research applications. The main advantages for the present application are due to a small target size and high spatial resolution achievable with IR cameras. The IR camera used in this study is FLIR ThermaCAM® SC3000 which has a thermal sensitivity of 20 mK at 30°C, an accuracy of 1% or 1°C for temperatures up to 150°C and 2% or 2°C for temperatures above 150°C. The quantum well infrared photon detector has a spectral range of 8 to 9 μm with a resolution of 320× 240 pixels. The system provides an automatic atmospheric transmission correction for temperature based on the input distance from the object, atmospheric temperature and relative humidity. A continuous electronic zoom (one to four times) is also provided. The system can acquire images in real time or at high speed (up to 750 Hz) with a reduction of the picture size so that each frame contains more than one image. The captured images are transferred to a dedicated PC with special built-in ThermaCAM® analysis software (provided by FLIR System). The target diameter was 2.5 mm. The spatial resolution of the system depends essentially on the spectral range (8 to 9 μm) of the IR camera, the instantaneous field of view of the camera and the microscope lens.

The infrared thermal imager, FLIR ThermaCAM® SC3000, was mounted near the machine turret and placed in view of the tool rake face during the cutting tests, as shown in Fig. 1. The camera was positioned at a distance of

Table 2 Summary of experimental conditions

Machine tool	Dean Smith & Grace Lathe machine (1910T lathe), UK
Workpiece material	AISI/SAE 4140 (23.9 HRC)
Workpiece size	200-mm external diameter and 2.5-mm tube thickness
Cutting insert	TCMW 16T304 (ISO grade P10)
Tool holder	STGCR 2020K-16
Cutting velocity, V_c	100, 197, 314, 395, 565 and 628 m/min
Feed rate, f	0.1 mm/rev
Depth of cut, a_p	2.5 mm
Environment	Dry orthogonal machining

35 cm from the tool workpiece interface in order to avoid any damage by the chips. The real temperature of an object depends on the emissivity of the material which is of particular concern when a thermal imaging camera is used. An accurate calibration of the thermographic system was carried out to find the emissivity values of the cutting tool material. The sample was heated to temperatures ranging from 100°C up to 900°C in an oven. A thermal imaging camera was used to read the insert temperature, and the emissivity was adjusted until the temperature reading of the thermal imager matched a thermocouple reading. For example, the average thermal emissivity of the uncoated cemented carbide tool insert was determined to be 0.48 at 700°C.

3 Finite element modelling

For FE analysis, plane strain conditions were assumed, as in almost all the previous studies [13, 14, 19–22, 27, 28, 31]. As the cutting width (2,500 μm) was much larger than the undeformed chip thickness (100 μm), this assumption was justified. In view of the large elastic modulus (534 GPa) of the tool material relative to that of the workpiece (210 GPa), the cutting tool was taken to be perfectly rigid.

The orthogonal cutting process was simulated using a two-dimensional model in ABAQUS/Explicit (version 6.6-1) to analyse turning of AISI/SAE 4140 (23.9 HRC) steel using a carbide cutting tool. Input requirements for the model included tool and workpiece geometry, tool and workpiece mechanical and thermal properties and boundary conditions. A two-dimensional model of the cutting edge, which includes chip formation, is shown in Fig. 2. A separation path was defined in the workpiece along which chip separation criteria were specified, thereby forming the chip. Fully coupled thermo-mechanical FE simulations are not able to follow the machining process up to steady-state conditions, as in order to keep the CPU time within reasonable limits, only a few milliseconds of the process can be simulated. Therefore, the workpiece length was taken as 2 mm, its height as 0.4 mm and a feed rate of 0.1 mm/rev, as shown in Fig. 2. The cutting tool had a clearance angle of 7°, rake angle of 0° and a height of 0.8 mm. The simulations were performed at six different cutting speeds of 100, 197, 314, 395, 565 and 628 m/min.

3.1 Material flow properties

According to a comparative analysis described by Shi and Liu [26], Johnson–Cook model is one of the most convenient material models which also produces excellent results describing the material behaviour and chip formation [45]. Also, Johnson–Cook model has been used successfully in high-speed machining region [17, 46, 47]. Therefore, in this work, the Johnson–Cook [48] constitutive model was used to predict the post-yield behaviour of AISI 4140 (23.9 HRC) steel. This model has been used in previous studies [49–51], particularly for AISI 4140 workpiece material. It is given by Eq. 1, as follows:

$$\overline{\sigma} = (A + B\overline{\varepsilon}^{n})\left[1 + C\ln\left(\frac{\dot{\overline{\varepsilon}}}{\dot{\overline{\varepsilon}}_0}\right)\right]\left[1 - \left(\frac{\theta - \theta_{room}}{\theta_{melt} - \theta_{room}}\right)^{m}\right] \quad (1)$$

where $\dot{\overline{\varepsilon}}$ is plastic strain rate, ε is equivalent plastic strain, $\dot{\overline{\varepsilon}}_0$ is reference strain rate, A is initial yield stress, B is hardening modulus, C is strain rate dependency coefficient, n is work hardening exponent, m is thermal softening coefficient, θ is the process temperature, θ_{melt} is the melting temperature of the workpiece and θ_{room} is the ambient temperature (25°C). An elastic–plastic workpiece material model was selected in ABAQUS/Explicit to describe the behaviour of the workpiece material as a function of strain, strain rate and temperature. The reference strain rate ($\dot{\overline{\varepsilon}}_0$) value was taken as 1.0 s^{-1} as suggested by Soo and Aspinwall [52] and Liang and Khan [53]. This reference value has also been used in many previous studies [28, 30, 31, 45, 54]. The actual material strain rate in cutting can achieve in order of 10^4 s^{-1} or higher. The Johnson–Cook flow model parameters for AISI 4140 were experimentally determined by Pantale et al. [55] as a function of strain, strain rate and temperature are as follows: A=595 MPa, B=580 MPa, C=0.023, n=0.133 and m=1.03. The thermo-physical properties of the workpiece and the cutting tool materials are listed in Table 3.

3.2 Chip separation criteria

There are two commonly used criteria, a geometrical criterion and an equivalent plastic strain criterion, to separate the chip from the machined surface in finite element analysis. Some authors have adopted the former separation criterion [29, 58]. The geometric criterion is convenient to use, but its physical meaning is not well established. Therefore, an equivalent plastic strain criterion was adopted in this study. This has become popular and effective in modelling chip separation of metal cutting [28, 33, 59]. According to this criterion, the material fails when the equivalent plastic strain reaches a critical value. This criterion was modelled in ABAQUS/Explicit according to a cumulative damage law given by Eq. 2 [48] as:

$$D = \sum\left(\frac{\Delta\overline{\varepsilon}}{\overline{\varepsilon}_{\mathrm{f}}}\right) \quad (2)$$

where D is the damage parameter, $\Delta\varepsilon$is increment of the equivalent plastic strain and $\varepsilon_f$is equivalent stain at failure. According to the Johnson–Cook model [48], $\Delta\varepsilon$ is updated

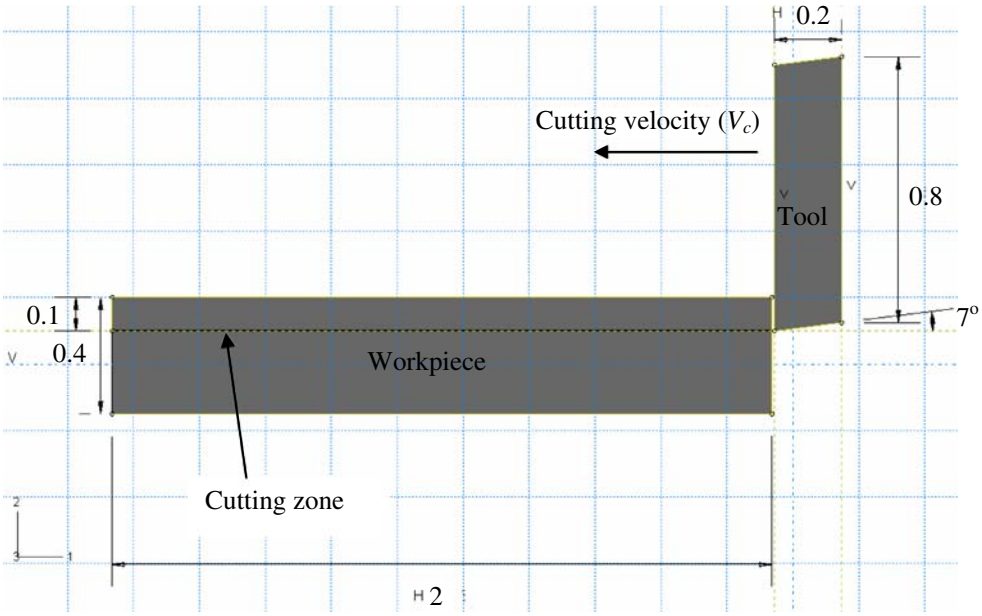

Fig. 2 Model and its dimensions used for cutting simulations (all dimensions are in millimetres)

at every load step, and ε_f is the equivalent strain at failure which is expressed by Eq. 3,

$$\bar{\varepsilon}_f = \left[D_1 + D_2 \exp\left(D_3 \frac{P}{\bar{\sigma}}\right)\right]\left[1 + D_4 \ln\left(\frac{\dot{\bar{\varepsilon}}}{\dot{\bar{\varepsilon}}_o}\right)\right]\left[1 + D_5\left(\frac{\theta - \theta_{room}}{\theta_{melt} - \theta_{room}}\right)\right] \tag{3}$$

and depends on the equivalent plastic strain rate $\dot{\bar{\varepsilon}}$, ratio $\dot{\bar{\varepsilon}}/\dot{\bar{\varepsilon}_0}$, ratio of hydrostatic (pressure) stress to equivalent stress $P/\bar{\sigma}$ and temperature (θ). The values of failure constants D_1, D_2, D_3, D_4 and D_5 were experimentally determined by Pantale et al. [55] for AISI 4140 steel as 1.5, 3.44, −2.12, 0.002 and 0.1, respectively. This cumulative damage model is used to perform chip detachment. It is based on the value of the equivalent plastic strain evaluated at element integration points; failure is assumed to occur when damage parameter D, given by Eq. 2, exceeds 1. When this condition is reached with an element, the stress components are set to zero at these points and remain zero for the rest of the calculations. The hydrostatic pressure

Table 3 Thermal and mechanical properties of the workpiece and the cutting tool materials [36, 56, 57]

At temperature (°C)		100	200	300	400	500	600	700	800
Properties of workpiece (AISI/SAE 4140)									
Young's modulus (GPa)	210								
Poisson's ratio	0.29								
Density (kg/m^3)	7,850								
Coefficient of expansion (μm m^{-1} °C^{-1})	13.7								
θ_{melt} (melting temperature, °C)	1,520								
θ_{room} (room temperature, °C)	25								
Thermal conductivity (W/m °C)		42.67	41.83	40.58	38.91	36.40	33.89	30.96	26.36
Specific heat capacity (J/kg °C)		473.10	489.80	506.60	527.50	548.41	577.70	611.27	690.82
Properties of cemented carbide cutting tool									
Young's modulus (GPa)	534								
Poisson's ratio	0.22								
Density (kg/m^3)	11,900								
Coefficient of expansion (μm m^{-1} °C^{-1})	–								
θ_{melt} (melting temperature, °C)	–								
θ_{room} (room temperature, °C)	25								
Thermal conductivity (W/m °C)		40.15	44.35	48.55	52.75	56.95	61.15	65.35	69.55
Specific heat capacity (J/kg °C)		346.01	358.01	370.01	382.01	394.01	406.01	418.01	430.01

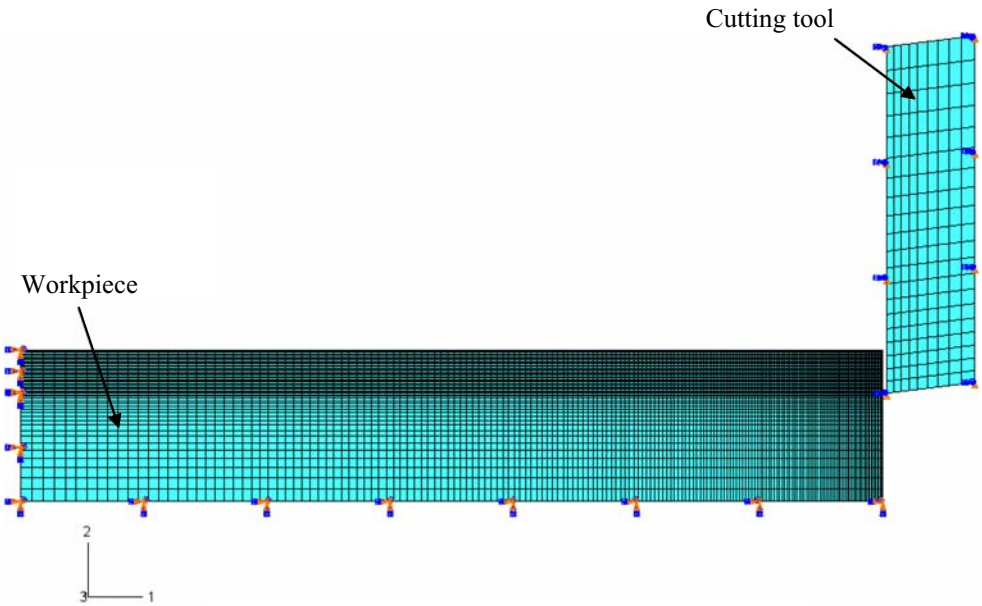

Fig. 3 Initial mesh configurations with constrains

stress is required to remain compressive; that is, if a negative hydrostatic pressure stress is computed in a failed material point during an increment, it is reset to zero [60].

3.3 Analysis

The cutting process is a dynamic event which produces large deformations within a few of increments, resulting in massive mesh distortion and sometimes in the termination of the simulation. It is critically important, therefore, to use adaptive meshing with fine-tuned parameters in order to simulate plastic flow over the cutting tool. This requires the intensity, frequency and sweeping of adaptive meshing to be optimally adjusted in order to maintain the stability of the mesh during the simulation of the cutting process.

An explicit dynamic procedure for a fully coupled thermal stress analysis method was used. It has the advantages of higher computational efficiency for large deformation and highly nonlinear problems such as machining. Machining, as a coupled thermal–mechanical process, generates heat to cause thermal effects which strongly influence mechanical behaviour. Thus, a fully coupled thermal stress analysis, in which a temperature solution and a stress solution proceed simultaneously, is applied.

3.4 Element type and boundary conditions

A four-node plane strain quadrilateral element, designated as CPE4RT in ABAQUS/Explicit, was used for the coupled temperature-displacement analysis with automatic hourglass control and reduced integration. Hourglass control was mandatory due to high element deformation. The workpiece consisted of 9,774 nodes and 9,180 elements, and the tool consisted of 210 nodes and 180 elements when undeformed chip thickness was 0.1 mm. The initial configuration of the model with constraints is shown in Fig. 3. The workpiece nodes on the bottom and left edge were constrained both vertically and horizontally, whilst the nodes on the left edge were also constrained vertically and horizontally. The tool was constrained against vertical

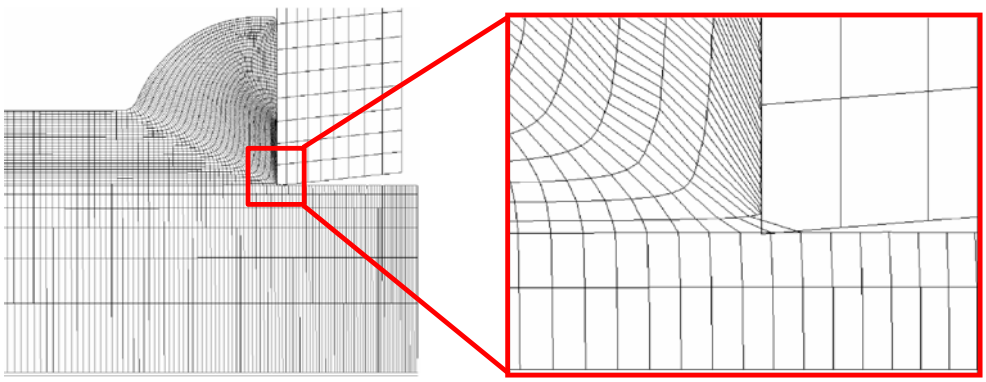

Fig. 4 Conditional link elements in the finite element model

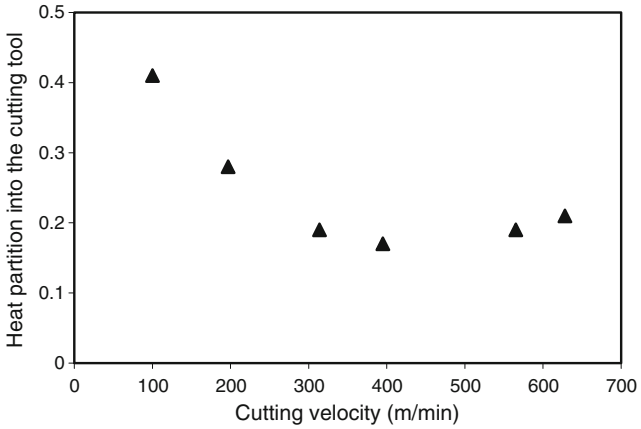

Fig. 5 Variation of heat partition with the cutting speed [36]

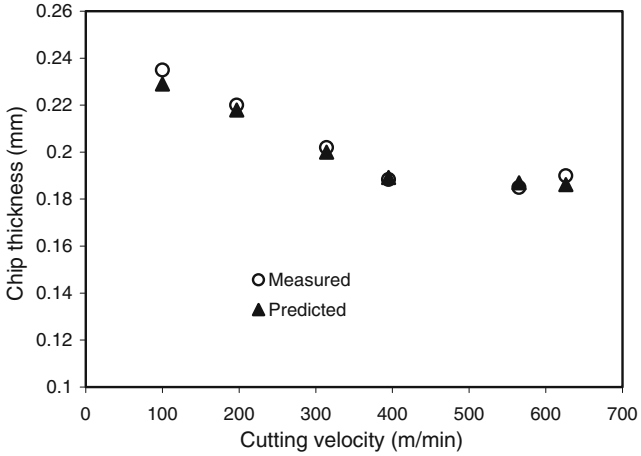

Fig. 7 Modelled and experimentally determined chip thickness

displacement and rotation. The dimensions of the workpiece were set to be large enough to maintain steady-state cutting. A higher mesh density was used in the potential chip regions, with mesh density decreasing towards the bottom edge of workpiece. In a coupled temperature-displacement analysis with ABAQUS/Explicit, displacements and temperatures are nodal variables. It is important to maintain the conditioning of the mesh, as machining is a dynamic event with considerable changes in geometry. This was achieved using an adaptive re-meshing technique. In this strategy, in order to save calculation time, the damage criterion is only applied to a localised contact zone, as shown in Fig. 4. The total simulation cutting time was 0.4 ms, with a length cut of 2 mm. The average computation time for each simulation was approximately 31 h on a 3.00-GHz workstation with 2-Gb RAM.

3.5 Modelling of tool–chip interface contact

The interaction between the cutting tool and the chip is a complex contact problem. Experimental observations have shown that there are usually two distinct regions on the rake face of the cutting tool, i.e. sticking and sliding regions. The interactions between the tool and the chip were analysed by considering contact behaviour which transmits normal and frictional stresses to the interfacial region. Modelling of the tool–chip interface friction was based on Coulomb's friction law which is defined by Eqs. 4 and 5. The formulation involves equivalent shear stress (τ_{max}), the friction coefficient (μ) and the frictional stress (τ_f) along the tool–chip interface. The friction module available in ABAQUS was employed in the friction model. This friction model has been used in many previous studies [27, 28, 33, 47], given as:

$$\tau_f = \mu p \quad \text{when} \quad \mu p < \tau_{max} (\text{sliding friction}) \tag{4}$$

$$\tau_f = \tau_{max} \quad \text{when} \quad \mu p < \tau_{max} (\text{sticking friction}) \tag{5}$$

where p is the normal stress along the tool rake face. The estimation of friction coefficient (μ) in Eq. 6 along the tool–chip interface for each cutting condition is based on the

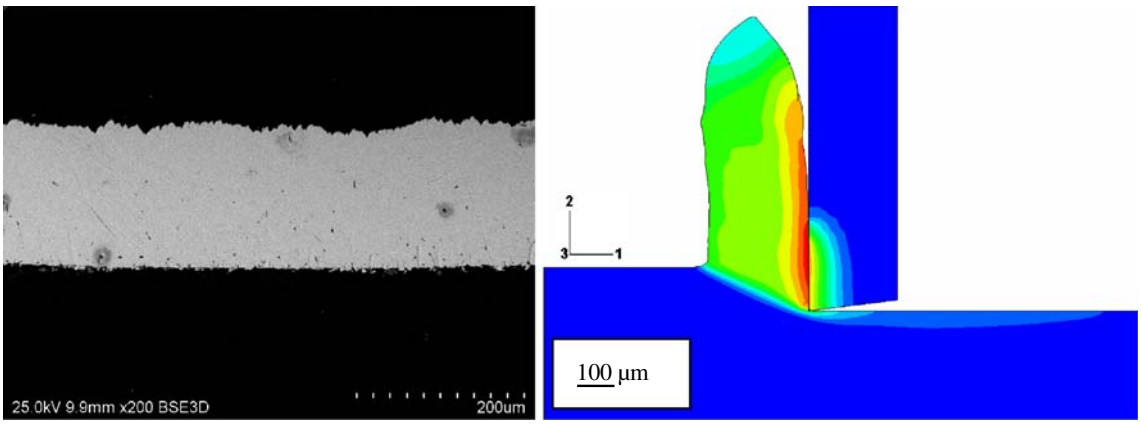

(a) **(b)**

Fig. 6 Chip morphology at 314 m/min **a** cutting test and **b** predicted

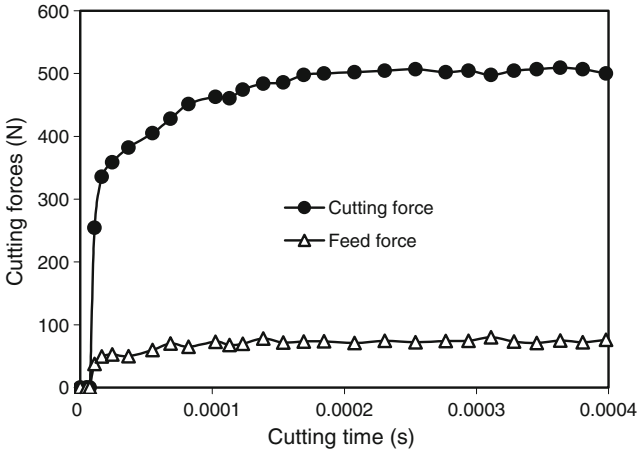

Fig. 8 FEM simulation cutting and feed forces history

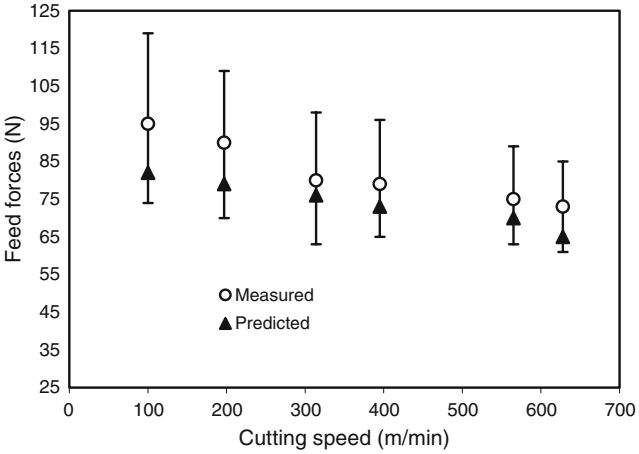

Fig. 10 Comparison of experimental and simulated feed forces (F_f)

experimental measurement of cutting force during orthogonal cutting as:

$$\mu = \frac{F_f \cos\gamma + F_c \sin\gamma}{F_c \cos\gamma - F_f \sin\gamma} \quad (6)$$

where F_c and F_f are the measured forces in the cutting velocity and feed directions, respectively, and γ is the rake angle. Equivalent shear stress (τ_{max}) can be estimated as the ratio of the measured feed force (when rake angle is equal to zero) to the seized area of the contact on the tool rake face [61].

3.6 Heat generation and heat partition between the tool and the chip

There are three sources for heat generation in metal cutting, material plastic deformation, chip friction and friction in the clearance face. Most of the plastic deformation energy is converted into heat, which is usually between 85% and 95% [19]. This percentage was taken as 90% in the current work, which has been widely used and reported in literature [19, 62, 63].

The heat generation module available in ABAQUS/Standard was employed for heat partition between the tool and the chip. Heat partition into the cutting tool was obtained using the hybrid FEM experimental approach as described by the authors in [36]. FEM was used as a tool in an inverse procedure aimed to identify the percentage of heat flowing into the cutting tool.

The algorithm was based on the following steps:

1. Compute for each experimental test the non-uniform heat flux value at the tool–chip interface.
2. Apply 100% of the heat flux in the FE model (uniform or non-uniform depending on contact phenomenon) as thermal load on the tool–chip contact area.
3. Reduce the applied heat flux until the measured and simulated temperatures are matched at the three points. This value is taken as heat partition into the cutting tool.

Figure 5 compares heat partition into the cutting tool (R_T) for uncoated carbide cutting tools from the combined FEM

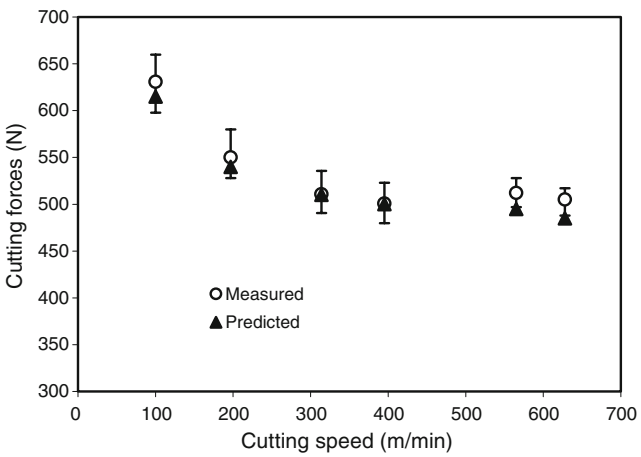

Fig. 9 Comparison of experimental and simulated cutting forces (F_c)

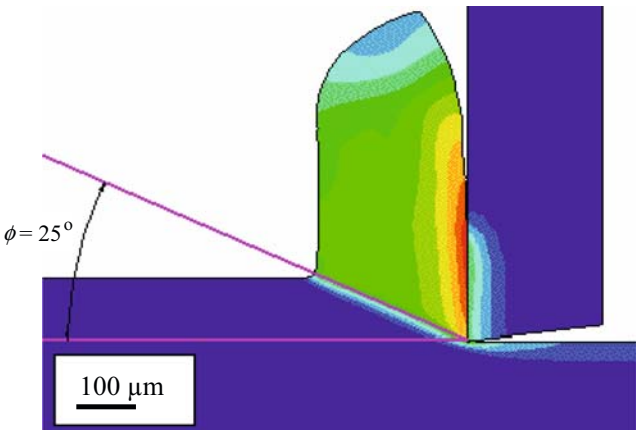

Fig. 11 Chip shape, shear angle and temperature distribution for cutting velocity=197 m/min and rake angle=0°

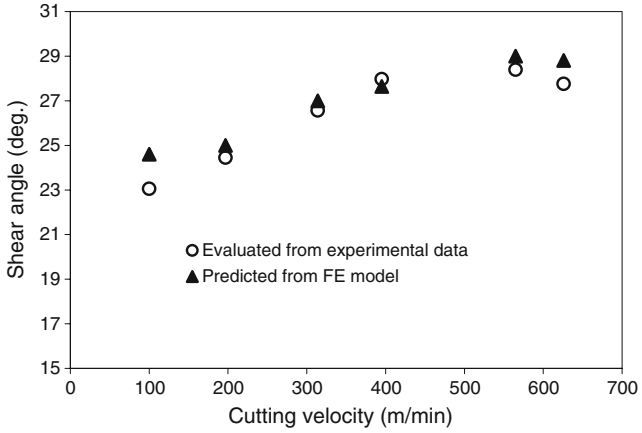

Fig. 12 Shear angle (ϕ) versus cutting velocity obtained from experiments and FE simulations

experimental approach and multiple-points matching. In the cutting speed range of 100 to 395 m/min, the heat partition coefficient obtained for uncoated cemented carbide tools varies from 41% down to 17%. When the cutting speed is increased above 395 m/min, the nature of the contact changes and the tool–chip contact length, and hence the contact area, increases for uncoated tools. As a consequence, Fig. 5 shows that the fraction of heat flowing into the uncoated cemented carbide tool gradually increases with the cutting speed and reaches 21% at 628 m/min.

Moreover, Fig. 5 shows a notable change in trend at 400 m/min. The mechanism for the change in heat partition when the cutting speed approaches 400 m/min needs further investigation. However, the tool–chip contact area has been found to be a dominant influence on heat partition. The cutting speed of 400 m/min represents the transition zone (between conventional and high-speed machining) where the trend for a reduction in the contact length with cutting speed, as experienced in conventional machining [64, 65], changes and starts to increase. This is driven by the change in the sliding contact phenomenon. This trend has been reported in an earlier work by Abukhshim et al. [66].

4 Results and discussion

4.1 Model validation

4.1.1 Deformed chip thickness

Figure 6a, b shows a scanning electron microscope (SEM) image of the chip obtained from the experiments and from simulation, respectively, when turning at 314 m/min. The FE model was first validated by comparing the experimentally obtained deformed chip thickness with FE results, as shown in Fig. 7. A good agreement between the predicted and the experimentally measured chip thickness was obtained. In general, the deformed chip thickness predicted by the model is lower than the experimental values. These deformed chip thickness data are used here to validate the FE model.

4.1.2 Cutting forces

Figure 8 shows the variation of the cutting and feed force components with time, as obtained from FE simulation at a cutting speed of 395 m/min. The cutting and feed forces had reached steady-state condition at the time of 0.00016 s. This justifies the use of 0.4-ms model run time in FE analysis.

As shown in Figs. 9 and 10, a good agreement is obtained between the predicted and measured forces for all cutting speeds. For the whole range of cutting speed, the relative percentage difference in the cutting force (F_c) prediction is 3% and 10% in the feed force (F_f). It can be seen that a better match is obtained for the cutting force, whilst the feed force is generally under-predicted for the whole range of cutting speeds. The discrepancy is in part due to the simplified Coulomb friction model employed to define the interaction between the tool and chip during machining. The model gives fairly good predictions in terms of the absolute error. Thus, the finite element model is considered to be satisfactorily validated and is used further to analyse the contribution of other relevant cutting parameters.

4.2 Shear angle

The shear angle (ϕ) is given as a function of rake angle and chip compression ratio, as in Eq. 7 [67].

$$\phi = \tan^{-1}\left(\frac{\cos\gamma}{\lambda_h - \sin\gamma}\right) \tag{7}$$

where γ is the rake angle and λ_h is the chip compression ratio defined as:

$$\lambda_h = \frac{t_c}{t} \tag{8}$$

where t_c is the chip thickness after cutting and t is the undeformed chip thickness. In this study, the primary shear

Table 4 Percentage differences of the shear angle between FE results and evaluated values (from experimental data)

Cutting speed (m/min)	100	197	314	395	565	628
Difference (%)	6.7	2.2	1.6	−1.1	2.1	3.7

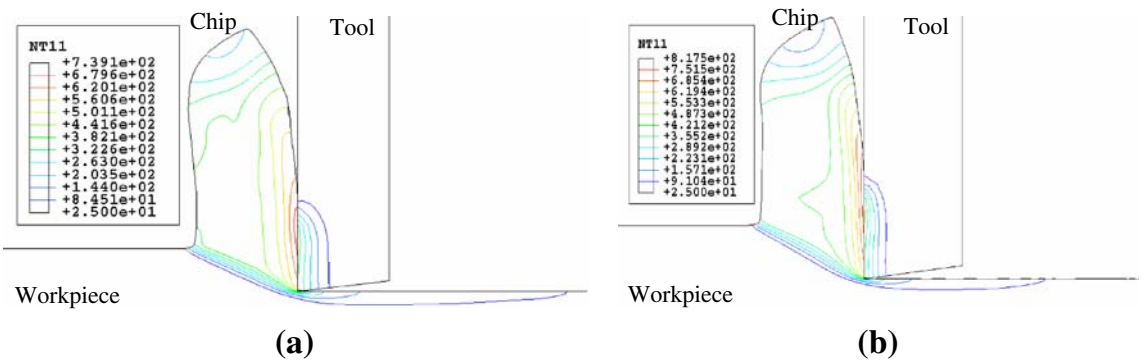

Fig. 13 Isothermal lines around the tool, chip and the workpiece for cutting speeds at **a** 314 and **b** 395 m/min

zone has been considered as a thin band. For each simulation, the shear angle is determined using a graphic CAD window (AutoCAD software) as shown in Fig. 11. Figure 12 shows a comparison between the predicted and the evaluated (from experimental data) shear angle. The shear angle increases with the cutting speed from 100 to 565 m/min and then stabilises at 628 m/min. The percentage differences of the shear angle between FE results and evaluated values (from experimental data) are given in Table 4.

4.3 Tool–chip interface temperature

4.3.1 Influences of cutting speed on temperature distributions

Figure 13a, b shows isotherms in the workpiece, the chip and the tool at the cutting speeds of 314 and 395 m/min, respectively, when modelling the uncoated carbide cutting tool. As can be seen, although the temperature around the middle of the shear plane is fairly constant, the temperature at the tool–chip interface is much higher. At 314-m/min cutting speed, a maximum temperature of 739°C was predicted in the chip sliding region on the tool–chip interface. At the point where the chip curled away from the rake face, the temperature decreased. The profiles of the isotherms were almost similar for all simulated conditions; however, the magnitude of the isotherms differed. The temperature distribution at the tool increased with the increase of cutting speed.

4.3.2 Comparison between numerical and experimental temperature values

The average tool–chip interface temperature increased, as expected, with higher cutting speed. Figure 14 shows the effect of cutting speed on the average tool–chip interface temperature for both FE simulations and the experimental data obtained from thermal imaging infrared camera. The tool–chip interface temperature output from the FE model was obtained by summation of nodal temperatures on the surface of the chip divided by the number of nodes.

As shown in Fig. 14, the average temperature at the tool–chip interface is generally lower than the temperature measured by the thermal imagining camera for each cutting speed. However, the average difference between model results and the experimental data was small for each cutting speed. Table 5 shows the percentage differences of the average tool–chip interface temperature predicted by FE model and experimental values.

4.4 Sensitivity of FE model to heat partition

As mentioned earlier, most researchers have assumed for FE models a value of heat partition into the cutting tool and chip as 50%. The validity of this assumption has to be tested. In order to determine the sensitivity of fraction of heat going into the cutting tool (R_T), 18 numerical tests were carried out at three different cutting speeds of 100, 395 and 628 m/min for six different R_T values of 0, 0.2, 0.4, 0.6, 0.8 and 1. This was to analyse the numerical sensitivity

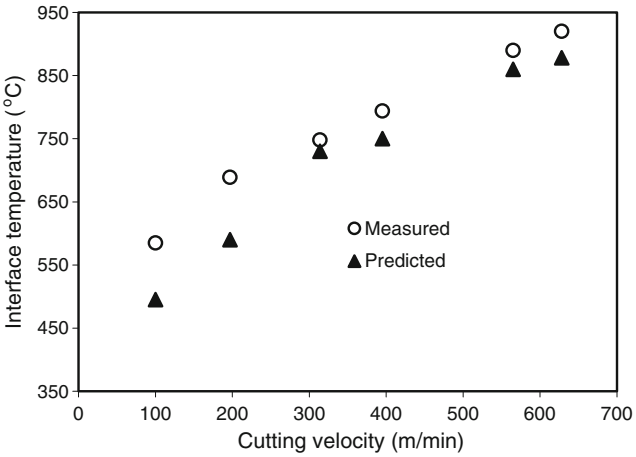

Fig. 14 Comparison between numerically predicted and experimentally measured tool–chip interface temperatures

Table 5 Percentage differences of the average tool–chip interface temperature between FE results and experimental values

Cutting speed (m/min)	100	197	314	395	565	628
Difference (%)	−15.3	−14.3	−2.4	−5.5	−3.3	−4.5

of R_T to chip morphology, temperatures, von Mises stresses and the tool–chip contact length.

4.4.1 Analysis of the tool–chip interface temperature

Figure 15 shows the effect of heat fraction into the tool (R_T) on temperature field and chip morphology. A smaller heat fraction (R_T) produces more curled and continuous chips, as more heat transfer into the chip causes an increase in the thermal stresses in the chip. It is also observed from Fig. 16 that a lower value of R_T decreases the temperature in the active part of the tool. Therefore, from an industrial point of view, it is interesting to choose a condition (such as coated tool materials with appropriate process parameters) which allows the removal of heat by the chip and hence save the tools from damage. From a practical point of view, the choice of a tool insert with poor thermal characteristics or a good thermal insulation can induce an entrapment of heat in the chip and therefore influence its morphology.

The average temperature along the chip tool contact length is shown in Fig. 16. It is observed that as heat partition into the cutting tool increases, the average temperature along the chip tool contact length increases by a small amount.

4.4.2 Analysis of the workpiece von Mises stress

Figure 17a–c shows the variation of equivalent (von Mises) stresses as a function of fraction of heat going into the cutting tool (R_T). It is observed that a decreasing R_T does not significantly influence the von Mises stress in the primary and secondary deformation zones.

However, the area where the effect is more pronounced is the tool–chip zone. In this area, higher values of von Mises stresses existed and the stress contours are extended into the machined surface of the workpiece as heat partition decreases. A lower value of R_T produces higher stresses in the workpiece. It is desirable, therefore, to choose a condition which allows a total removal of heat by the chip in order to avoid damage to the cutting tools.

4.4.3 Analysis of the tool–chip contact length

The tool–chip contact length along the rake face of the cutting tool can be affected by mechanics of machining, heat generation and heat partition into the cutting tool. In this study, the tool–chip contact length of the worn carbide cutting inserts was obtained at different cutting speeds from a SEM. Sample SEM images of the worn insert are shown

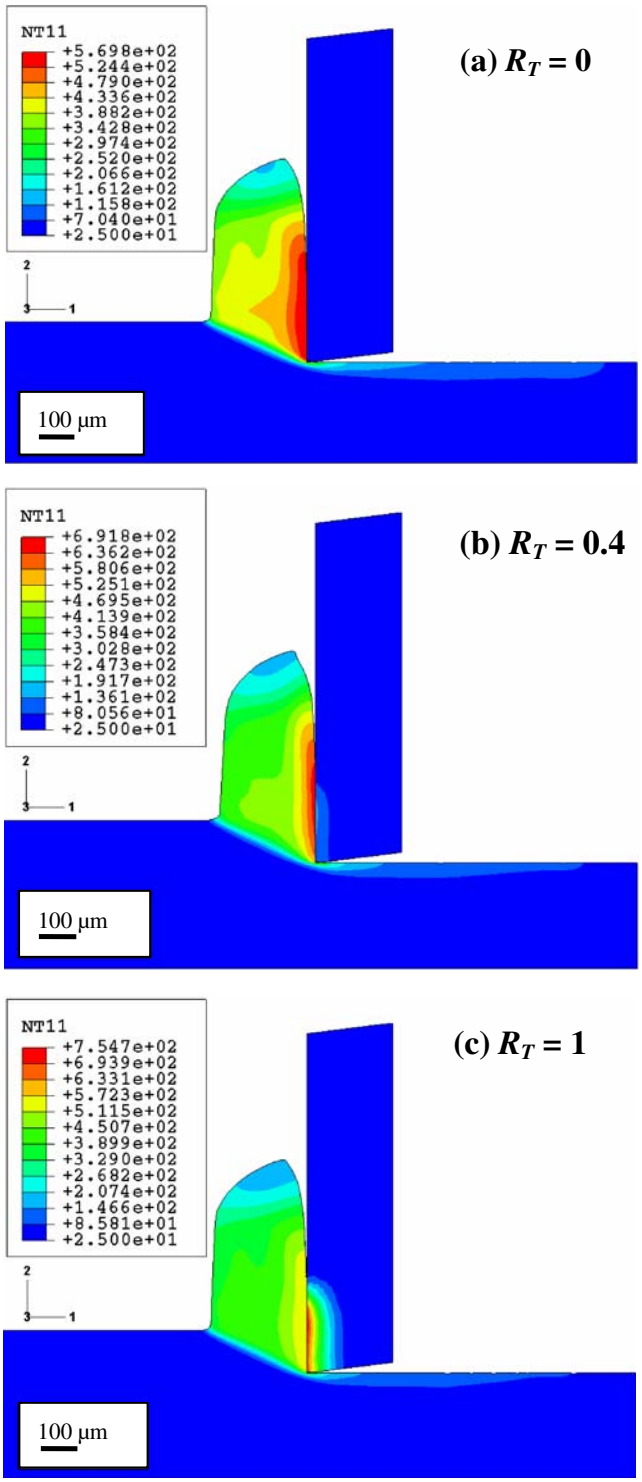

Fig. 15 Effect of heat fraction R_T on temperature distribution (°C) at 100 m/min **a** R_T=0, **b** R_T = 0.4 and **c** R_T=1

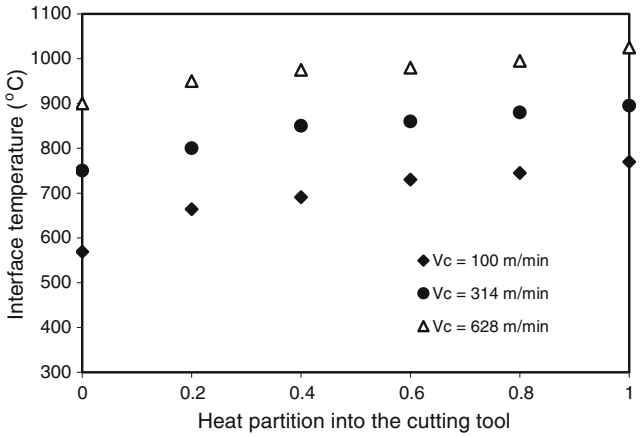

Fig. 16 Average tool–chip interface temperature versus heat partition into the cutting tool

in Fig. 18. Figure 19 presents the calculated tool–chip contact length obtained from the SEM images of the worn inserts at different cutting speeds for carbide cutting tools. It is observed that the contact length is significantly affected by the cutting speed.

The effect of heat partition into the cutting tool (R_T) on the tool–chip contact length is shown in Fig. 20 for cutting speeds of 100, 395 and 628 m/min. It is observed that variation of R_T also influences the tool–chip contact length which increases with increasing R_T. Comparing the tool–chip contact length within the bounds of heat partition (R_T= 0 and R_T=1), the average tool–chip contact length increases by 25%, 37% and 36% for cutting speeds of 100, 314 and 628 m/min, respectively.

The sensitivity analysis appears to underestimate the tool–chip contact length (inferring from Figs. 5, 19 and 20). Prediction of contact phenomenon strongly depends on the friction rules and heat flux distribution. Modelling of the tool–chip contact length can be further improved, as in this

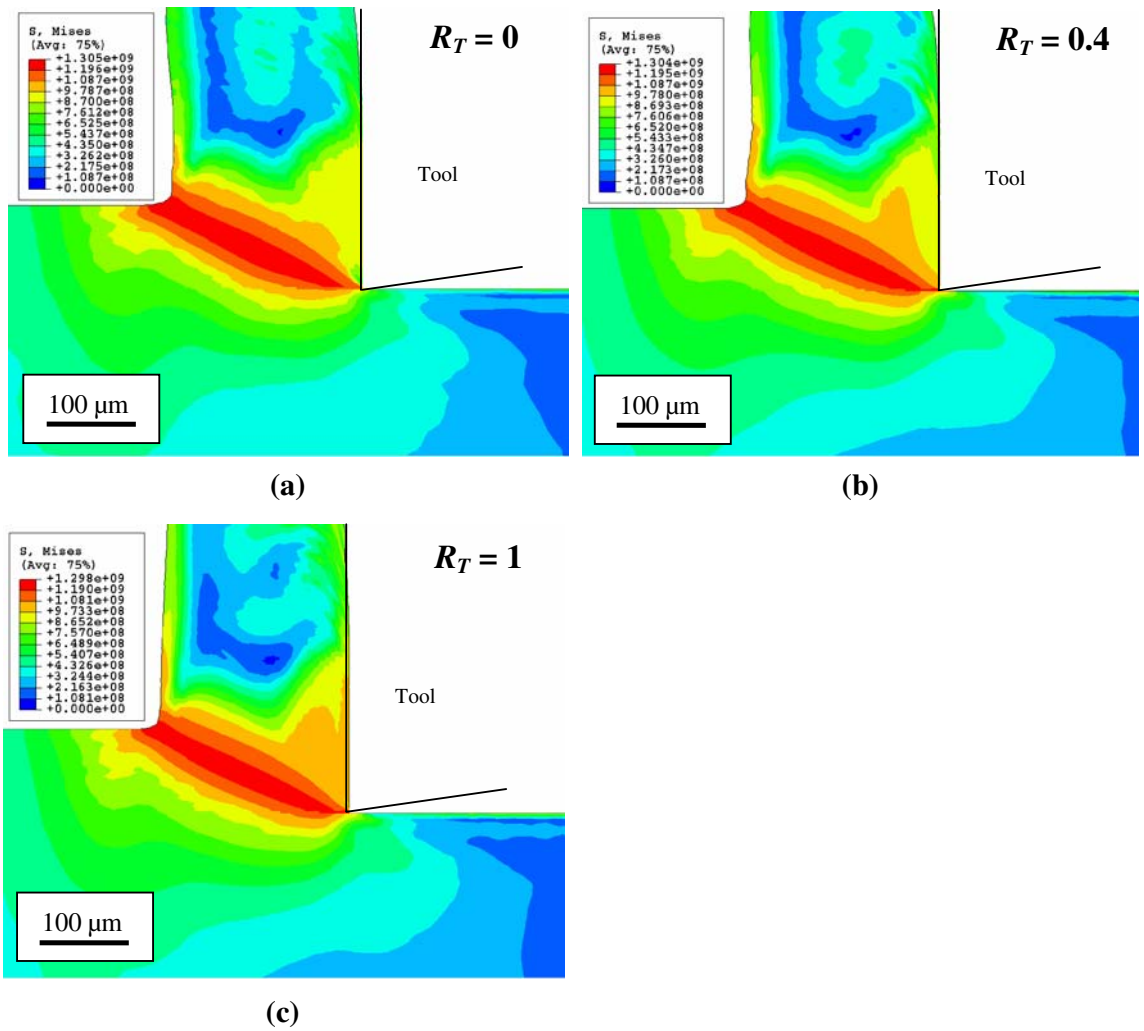

Fig. 17 Effect of heat fraction R_T on the equivalent (von Mises) stress (N/m^2) at 100 m/min **a** R_T=0, **b** R_T=0.4 and **c** R_T=1

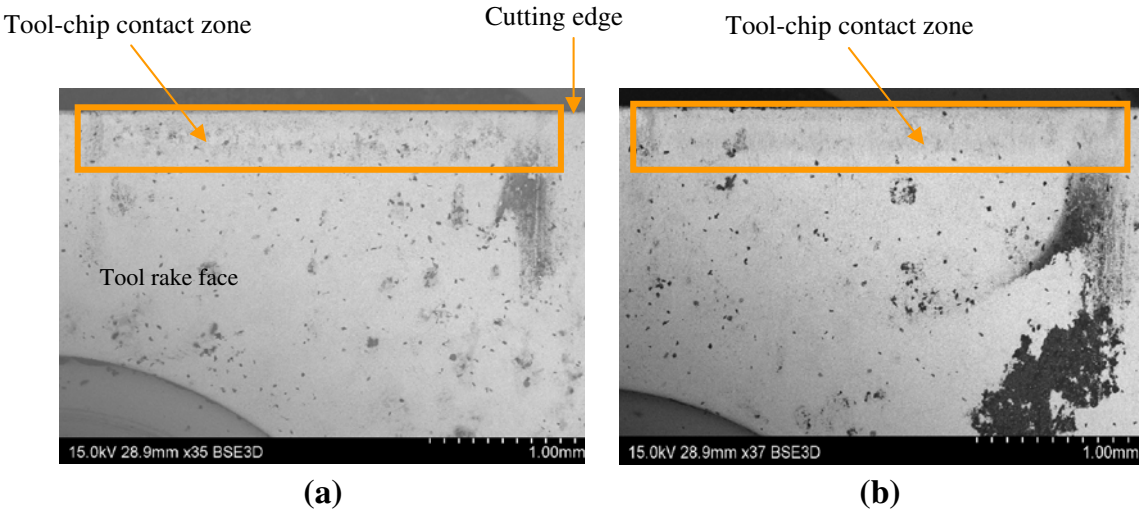

Fig. 18 Scanning Electron Microscope images of the tool–chip length of uncoated carbide cutting tool at cutting speeds of **a** 100 m/min and **b** 628 m/min

paper, a simplified Coulomb friction model was employed to define the interaction between the tool and the chip during machining. Improvements are needed in modelling the material behaviour and contact algorithms.

Moreover, the sensitivity analysis as presented shows how cutting temperature and tool–chip contact length correlate with heat partition. In an earlier publication, heat partition was found to be strongly dependant on contact phenomenon such as the tool–chip contact area [36]. The tool–chip contact area follows a similar trend to the tool–chip contact length as shown in Fig. 19.

5 Conclusions

This paper presents results of a coupled thermo-mechanical analysis with the aim of studying the influence of the fraction of heat going into the tool on the cutting process using a FE model. The model is based on realistic heat partition established by iteratively reducing the heat flux in order to match the predicted and experimental temperatures at multiple points in the contact zone. The deformed chip thickness, cutting forces, shear angle and the tool–chip interface temperature predicted by the FE model have shown good agreement with experimentally measured data, thereby validating the model.

The model is used to test the widely accepted practice of assuming a heat partition value in FE models. From a practical point of view, it is required to choose conditions which allow the removal of heat by the chip in order to save the cutting tools from thermal damage. In this study, the effect of heat partition into the cutting tool (R_T) on the tool–chip interface temperatures, von Mises stresses and the tool–chip contact length is quantified. If a low fraction of

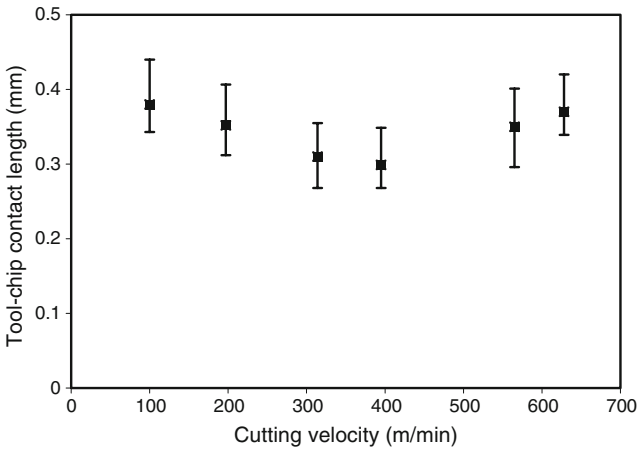

Fig. 19 Variation of the experimentally measured tool–chip contact length with the cutting speed

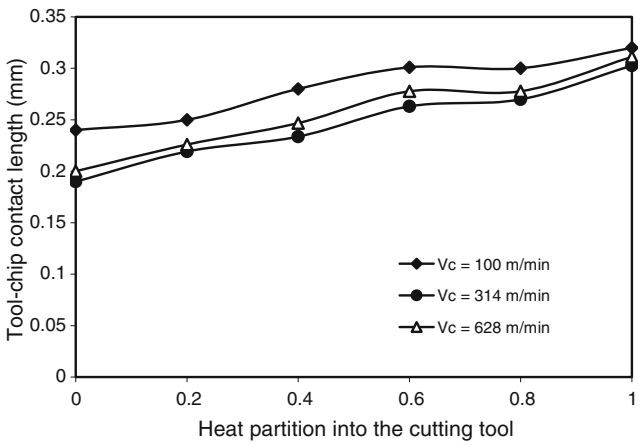

Fig. 20 Effect of heat fraction R_T on the tool–chip contact length (mm)

heat going into the cutting tool is assumed, the tool side tool–chip interface temperature is significantly reduced. The results also show that heat partition can significantly modify the tool–chip contact area and hence affect the capability of FE model to adequately represent the process. Based on these results, it can be concluded that the machining process needs an accurate determination of heat partition between the tool and the chip. Heat partition should not be treated as a non-critical input which can be routinely assumed, as is the case with most FE models previously developed and used to simulate machining processes.

Nomenclature

A, B, C, m, n	Johnson–Cook flow stress model parameters
a_p	Depth of cut (mm)
D_1, D_2, D_3, D_4, D_5	Johnson–Cook damage law parameters
F_c	Cutting force (N)
F_f	Feed force (N)
f	Feed rate (mm/rev)
p	Normal stress acting on the tool (N/mm^2)
R_T	Fraction of heat conducted into the tool
t	Undeformed chip thickness (mm)
t_c	Actual chip thickness (mm)
V_c	Cutting velocity (m/min or m/s as defined)
γ	Rake angle (deg)
λ_h	Chip compression ratio=t_c/t
μ	Friction coefficient
θ	Operating temperature (°C)
θ_{melt}	Melting temperature of the workpiece (°C)
θ_{room}	Room temperature (°C)
ϕ	Shear angle (deg)
ρ	Density (kg/m^3)
τ_f	Frictional stress along the tool–chip interface (N/mm^2)
τ_{max}	Equivalent shear flow stress (N/mm^2)
$\overline{\sigma}$	Equivalent flow stress or the workpiece material (N/mm^2)
$\dot{\overline{\varepsilon}}$	Plastic strain rate (s^{-1})
$\overline{\varepsilon}$	Equivalent plastic strain
$\dot{\overline{\varepsilon_0}}$	Reference strain rate (s^{-1})
$\Delta\overline{\varepsilon}$	Increment of the equivalent plastic strain
$\overline{\varepsilon}_f$	Equivalent strain at failure

References

1. Blok H (1938) Theoretical study of temperature rise at surfaces of actual contact under oiliness lubricating conditions. Proceedings of General Discussion on Lubrication and Lubricants, Institute of Mechanical Engineers London, pp 222–235
2. Chao BT, Trigger KJ (1955) Temperature distribution at the tool–chip interface in metal cutting. Trans ASME 72:1107–1121
3. Komanduri R, Hou ZB (2001) Thermal modeling of the metal cutting process Part II: temperature rise distribution due to frictional heat source at the tool–chip interface. Int J Mech Sci 43:57–88. doi:10.1016/S0020-7403(99)00104-6
4. Huang Y, Liang SY (2005) Cutting temperature modeling based on non-uniform heat intensity and partition ratio. Min Sci Technol 9:301–323
5. Karpat Y, Özel T (2006) Predictive analytical and thermal modeling of orthogonal cutting process—part I: predictions of tool forces, stresses, and temperature distributions. Trans ASME J Manuf Sci Eng 128:435–444. doi:10.1115/1.2162590
6. Karpat Y, Özel T (2006) Predictive analytical and thermal modeling of orthogonal cutting process—part II: effect of tool flank wear on tool forces, stresses, and temperature distributions. Trans ASME J Manuf Sci Eng 128:445–453. doi:10.1115/1.2162591
7. Loewen EG, Shaw MC (1954) On the analysis of cutting tool temperatures. Trans ASME 71:217–231
8. Takeuchi Y, Sakamoto M, Sata T (1982) Improvement in the working accuracy of an NC lathe by compensating for thermal expansion. Precis Eng 4(1):19–24. doi:10.1016/0141-6359(82)90109-X
9. Wright PK, McCormick SP, Miller TR (1980) Effect of rake face design on cutting tool temperature distributions. ASME J Eng Ind 102(2):123–128
10. Casto LS, Valvo LE, Micari F (1989) Measurement of temperature distribution within tool in metal cutting. Experimental tests and numerical analysis. J Mech Work Technol 20:35–46. doi:10.1016/0378-3804(89)90016-8
11. Grzesik W, Nieslony P (2003) A computational approach to evaluate temperature and heat partition in machining with multilayer coated tools. Int J Mach Tools Manuf 43:1311–1317. doi:10.1016/S0890-6955(03)00160-3
12. Abukhshim NA, Mativenga PT, Sheikh MA (2005) Investigation of heat partition in high speed turning of high strength alloy steel. Int J Mach Tools Manuf 45:1687–1695. doi:10.1016/j.ijmachtools.2005.03.008
13. Shih AJ (1996) Finite element analysis of orthogonal metal cutting mechanics. Int J Mach Tools Manuf 36:255–273. doi:10.1016/0890-6955(95)98765-Y
14. Lei S, Shin YC, Incropera FP (1999) Thermo-mechanical modeling of orthogonal machining process by finite element analysis. Int J Mach Tools Manuf 39:731–750. doi:10.1016/S0890-6955(98)00059-5
15. Xie L-J, Schmidt J, Schmidt C et al (2005) 2D FEM estimate of tool wear in turning operation. Wear 258:1479–1490. doi:10.1016/j.wear.2004.11.004
16. Arrazola PJ, Ugarte D, Dominguez X (2008) A new approach for the friction identification during machining through the use of finite element modeling. Int J Mach Tools Manuf 48:173–183. doi:10.1016/j.ijmachtools.2007.08.022
17. Arrazola PJ, Villar A, Ugarte D et al (2007) Serrated chip prediction in finite element modeling of the chip formation process. Min Sci Technol 11:367–390
18. Reginaldo TC, Ng E-G, Elbestawi MA (2007) Tool wear when turning hardened AISI 4340 with coated PCBN tools using finishing cutting conditions. Int J Mach Tools Manuf 47:263–272. doi:10.1016/j.ijmachtools.2006.03.020

19. Shet C, Deng X (2000) Finite element analysis of the orthogonal metal cutting process. J Mater Process Technol 105:95–109. doi:10.1016/S0924-0136(00)00595-1
20. Shet C, Deng X, Bayoumi AE (2003) Finite element simulation of high-pressure water-jet assisted metal cutting. Int J Mech Sci 45:1201–1228. doi:10.1016/S0020-7403(03)00142-5
21. Shi G, Deng X, Shet C (2002) A fnite element study of the efect of friction in orthogonal metal cutting. Finite Elem Anal Des 38:863–883. doi:10.1016/S0168-874X(01)00110-X
22. Shet C, Deng X (2003) Residual stresses and strains in orthogonal metal cutting. Int J Mach Tools Manuf 43:573–587. doi:10.1016/S0890-6955(03)00018-X
23. Shi J, Liu CR (2006) On predicting chip morphology and phase transformation in hard machining. Int J Adv Manuf Technol 27:645–654. doi:10.1007/s00170-004-2242-0
24. Shi J, Liu CR (2005) On predicting softening effects in hard turned surfaces—part II: finite element modeling and verification. Trans ASME 127:484–491. doi:10.1115/1.1843166
25. Kai L, Melkote SN (2006) Material strengthening mechanisms and their contribution to size effect in micro-cutting. Trans ASME 128:730–738
26. Shi J, Liu CR (2004) The influence of material models on finite element simulation of machining. J Manuf Sci Eng 126:849–857. doi:10.1115/1.1813473
27. Li K, Gao X-L, Sutherland JW (2002) Finite element simulation of the orthogonal metal cutting process for qualitative understanding of the effects of crater wear on the chip formation process. J Mater Process Technol 127:309–324. doi:10.1016/S0924-0136(02)00281-9
28. Mabrouki T, Rigal J-F (2006) A contribution to a qualitative understanding of thermo-mechanical effects during chip formation in hard turning. J Mater Process Technol 176:214–221. doi:10.1016/j.jmatprotec.2006.03.159
29. Ng EG, Aspinwall DK, Brazil D et al (1999) Modelling of temperature and forces when orthogonally machining hardened steel. Int J Mach Tools Manuf 39:885–903. doi:10.1016/S0890-6955(98)00077-7
30. Zong WJ, Li D, Cheng K et al (2007) Finite element optimization of diamond tool geometry and cutting-process parameters based on surface residual stresses. Int J Adv Manuf Technol 32:666–674. doi:10.1007/s00170-005-0388-z
31. Mohamed AN, Ng EG, Elbestawi MA (2007) Modelling the effects of tool-edge radius on residual stresses when orthogonal cutting AISI 316 L. Int J Mach Tools Manuf 47:401–411. doi:10.1016/j.ijmachtools.2006.03.004
32. Guo YB, Yen DW (2004) A FEM study on mechanisms of discontinuous chip formation in hard machining. J Mater Process Technol 155–156:1350–1356. doi:10.1016/j.jmatprotec.2004.04.210
33. Ng EG, Aspinwall DK (2002) Modelling of hard part machining. J Mater Process Technol 127:222–229. doi:10.1016/S0924-0136(02)00146-2
34. Barry J, Byrne G (2002) The mechanisms of chip formation in machining hardened steels. Trans ASME J Manuf Sci Eng 124:528–535. doi:10.1115/1.1455643
35. Kishawy HA, Deiab IM, Haglund AJ (2007) Arbitrary Lagrangian Eulerian analysis on cutting with a honed tool. Proc Inst Mech Eng, Part B J Eng Manuf 222:155–162
36. Akbar F, Mativenga PT, Sheikh MA (2008) An evaluation of heat partition in high-speed turning of AISI/SAE 4140 steel with uncoated and TiN-coated tools. Proc Inst Mech Eng, Part B J Eng Manuf 222:759–771
37. Boothroyd G (1963) Temperatures in orthogonal metal cutting. Proc Inst Mech Eng 177(29):789–810. doi:10.1243/PIME_PROC_1963_177_058_02
38. Wanigarathne PC, Kardekar AS, Dillon OW et al (2005) Progressive tool-wear in machining with coated grooved tools and its correlation with cutting temperature. Wear 259:1215–1224. doi:10.1016/j.wear.2005.01.046
39. Kwon P, Schiemann T, Kountanya R (2001) An inverse estimation scheme to measure steady-state tool–chip interface temperatures using an infrared camera. Int J Mach Tools Manuf 41:1015–1030. doi:10.1016/S0890-6955(00)00113-9
40. Davies MA, Cao Q, Cooke AL et al (2003) On the measurement and prediction of the temperature fields in machining. Ann CIRP 52:77–80. doi:10.1016/S0007-8506(07)60535-6
41. M'Saoubi R, Chandrasekaran H (2004) Investigation of the effects of tool micro-geometry and coating on tool temperature during orthogonal turning of quenched and tempered steel. Int J Mach Tools Manuf 44:213–224. doi:10.1016/j.ijmachtools.2003.10.006
42. Davies MA, Cooke AL, Larsen ER (2005) High bandwidth thermal microscopy of machining AISI 1045 steel. Ann CIRP 54 (1):63–66. doi:10.1016/S0007-8506(07)60050-X
43. Davies MA, Ueda T, M'Saoubi R et al (2007) On the measurement of temperature in material removal processes. Ann CIRP 56(2):581–604. doi:10.1016/j.cirp.2007.10.009
44. Filice L, Umbrello D, Beccari S et al (2006) On the FE codes capability for tool temperature calculation in machining processes. J Mater Process Technol 174:286–292. doi:10.1016/j.jmatprotec.2006.01.012
45. Belhadi S, Mabrouki T, Rigal JF et al (2005) Experimental and numerical study of chip formation during straight turning of hardened AISI4340 steel. Proc ImechE, Part B J Eng Manuf 219:515–524. doi:10.1243/095440505X32445
46. Özel T, Zeren E (2005) Finite element modeling of stresses induced by high speed machining with round edge cutting tools. Proceedings of IMECE, ASME International Mechanical Engineering Congress & Exposition, pp 1–9
47. Ng EG, El-Wardany TI, Dumitrescu M et al (2002) Physics-based simulation of high speed machining. Min Sci Technol 6(3):301–329
48. Johnson GR, Cook WH (1985) Fracture characteristics of three metals subjected to various strains, strain rates, temperatures and pressures. Eng Fract Mech 21(1):31–48. doi:10.1016/0013-7944(85)90052-9
49. Bacaria J-L, Dalverny O, Caperaa S (2001) A three-dimensional transient numerical model of milling. Proc Inst Mech Eng, Part B J Eng Manuf 215:1147–1150
50. Joyot P, Rakotomalala R, Pantale O et al (1998) A numerical simulation of steady state metal cutting. Proc Inst Mech Eng 212:331–341. doi:10.1243/0957650981536907
51. Rakotomalala R, Joyot P (1993) Arbitrary Lagrangian–Eulerian thermomechanical finite-element model of material cutting. Commun Numer Methods Eng 9:975–987. doi:10.1002/cnm.1640091205
52. Soo SL, Aspinwall DK (2007) Developments in modelling of metal cutting processes. Proc IMechE Part L, J Mater Des Appl 221:197–211
53. Liang R, Khan AS (1999) A critical review of experimental results and constitutive models for BCC and FCC metals over a wide range of strain rates and temperatures. Int J Plast 15(9):963–980. doi:10.1016/S0749-6419(99)00021-2
54. Outeiro JC, Umbrello D, M'Saoubi R (2006) Experimental and numerical modelling of the residual stresses induced in orthogonal cutting of AISI 316 L steel. Int J Mach Tools Manuf 46(14):1786–1794. doi:10.1016/j.ijmachtools.2005.11.013
55. Pantale O, Bacaria J-L, Dalverny O et al (2004) 2D and 3D numerical models of metal cutting with damage effects. Comput Methods Appl Mech Eng 193:4383–4399. doi:10.1016/j.cma.2003.12.062
56. Woolman J, Mottram RA (1964) The mechanical and physical properties of the British standard En steels, vol 1. Pergamon, London

57. Childs T, Maekawa K, Obikawa T et al (2000) Metal machining theory and applications. Arnold, London (a member of Hodder and Headline group)
58. Liu CR, Guo YB (2000) FEM analysis of residual stresses on the sequential machined surface. J Mech Sci 42:1069–1089. doi:10.1016/S0020-7403(99)00042-9
59. Shih AJ (1995) Finite element simulation of orthogonal metal cutting. J Eng Ind 11:84–93. doi:10.1115/1.2803283
60. Hibbitt K Sorensen (2006) ABAQUS/explicit user's manual: version 6.6-1, ABAQUS
61. Trent EM (1984) Metal cutting, 2nd edn. Butterworth, London
62. Mamalis AG, Horvath M, Branis AS et al (2001) Finite element simulation of chip formation in orthogonal metal cutting. J Mater Process Technol 110(1):19–27. doi:10.1016/S0924-0136(00)00861-X
63. Liu CR, Guo YB (2000) Finite element analysis of the effect of sequential cuts and tool–chip friction on residual stresses in a machined layer. Int J Mech Sci 42:1069–1086. doi:10.1016/S0020-7403(99)00042-9
64. Gad GS, Armarego JA, Smith AJR (1992) Tool–chip contact length in orthogonal machining and its importance in tool temperature predictions. Int J Prod Res 30(3):485–501. doi:10.1080/00207549208942907
65. Sadik MI, Lindstrom B (1993) The role of tool–chip contact length in metal cutting. J Mater Process Technol 37:613–627. doi:10.1016/0924-0136(93)90122-M
66. Abukhshim NA, Mativenga PT, Sheikh MA (2004) An investigation of the tool–chip contact length and wear in high-speed turning of EN19 steel. Proc Inst Mech Eng, Part B J Eng Manuf 218:889–903
67. Merchant ME (1945) Mechanics of the metal cutting process. I. Orthogonal cutting and type 2 chip. J Appl Phys 16(5):267–275. doi:10.1063/1.1707586